RESEARCH ARTICLE

Hydrothermal and peat-derived carbons as electrode materials for high-efficient electrical double-layer capacitors

M. Härmas[1] · R. Palm[1] · T. Thomberg[1] · R. Härmas[1] · M. Koppel[1] · M. Paalo[1] · I. Tallo[1] · T. Romann[1] · A. Jänes[1] · E. Lust[1]

Abstract

Different micro–mesoporous carbons derived from D-glucose (GDC), granulated white sugar (WSDC) and highly decomposed Estonian peat (PDC) were synthesized using hydrothermal carbonization and direct activation methods. The resulting carbonaceous materials were activated using chemical (KOH and $ZnCl_2$) and physical (CO_2) activation methods. The electrochemical characteristics of the electrical double-layer capacitors (EDLCs) based on 1 M Et_3MeNBF_4 solution in acetonitrile and $EtMeImBF_4$ were measured using two-electrode cells. The EDLCs assembled had specific capacitances from 20 up to 158 ± 18 F g^{-1} (in $EtMeImBF_4$) and phase angle values from $-65°$ to $-88°$ (at low frequencies). The characteristic time constant values vary more than 10 times. Applying constant power discharge method, very high energy and power densities (34 W h kg^{-1} at 10 kW kg^{-1}) for activated carbon powders-based EDLCs have been measured. Fitting of impedance data showed that enhanced mesoporosity reduces the adsorption and mass-transfer resistance values.

Graphic abstract
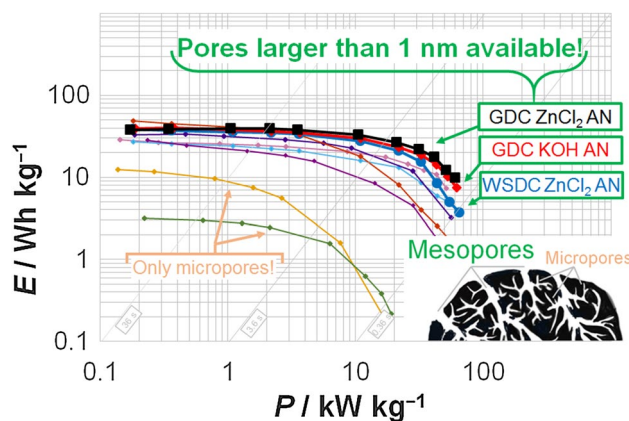
✉ T. Thomberg
thomas.thomberg@ut.ee

Extended author information available on the last page of the article

1 Introduction

Electrochemical energy conversion and storage devices are the basis of a sustainable energy economy of the future [1–12]. Whatever method is used to generate electrical energy (solar photovoltaic cells, wind turbines, etc.), energy storage is inevitable for grid stabilization. Supercapacitors can store energy as electrical charge, Li-ion

and Na-ion batteries can store energy as electrochemically active compounds [1–6]. Due to the fundamental differences in the mechanism of energy storage processes, Gibbs electrostatic adsorption in supercapacitors and faradic oxidation/reduction reactions in Li-ion and Na-ion batteries and polymer electrolyte membrane or solid oxide electrolysis cells, the characteristic charging/discharging times (and relaxation times) are very different [3–21].

In electrical double-layer capacitors (EDLC), the characteristic relaxation times can be very short if the highly micro–mesoporous electrodes have been used [8, 13–21]. Thus, the EDLCs can generate very short but very high power density current pulses without degradation of the electrode materials [1–4]. However, for Li-ion and Na-ion batteries, the very high-density current pulses are harmful and quick degradation of devices is possible [5–7]. The polymer membrane electrolyte electrolysers or CO_2 and H_2O co-electrolysers are under intensive studies with the main direction to prepare devices resistive for current pulses and quick cyclation of cell potential [11, 22]. Thus, for very effective pulsating energy storage (corresponding to the quickly pulsating solar or wind energy), the electrolysers should have very quickly inflecting polarizabilities of electrodes. Therefore, the electrodes should have very short characteristic relaxation times, i.e. very high oxidation/reduction rate constant values at devices electrodes [22–24]. In addition, the very flexible hydrogen accumulation/storage/release devices should be developed and applied [25, 26]. Solid oxide electrolysers usually cannot be used in energy recuperation systems without introducing intermediate energy storage devices like high power density EDLCs and pulse batteries.

For effective long-lasting application of the energy storage electrodes/devices, the alternative extremely high current pulses should be avoided. However, for quick release of electricity, the highly micro–mesoporous electrodes with very good electrical conductivity of a matrix material as well as current collectors should be used [27–29]. In principle, the series resistance (sometimes known as high-frequency series resistance) consisting of the current collector resistances, electrode matrix resistance and contact resistance value between electrode layer and current collector and electrolyte layer (so-called volume resistance in porous electrode matrix) determines the total series resistance of a device [8, 18]. In addition, the mass-transfer and adsorption resistance values are very important parameters determining the energy accumulation/liberation rate. Lipophilicity of the electrode and separator materials and viscosity of an electrolyte are very critical parameters as well [8, 27, 29–31]. It is clear that the viscosity of electrolyte solution increases very noticeably from H_2O-based electrolytes to propylene carbonate, ethylene carbonate and future to various ionic liquids and/

or ionic liquids mixtures, increasing the series resistance of the two-electrode cells [8, 27–29, 32–42].

In addition, the electrolyte conductivity increases and Debye screening length (solvated ion diameter) decreases with the rise of electrolyte concentration as given by Eq. (1)

$$\lambda_D = \left(\frac{\varepsilon_r \varepsilon_0 k_B T}{\sum_i \rho_{\infty i} e^2 z_i^2} \right)^{1/2} \tag{1}$$

where $\rho_{\infty i}$ is the number density of ion type i, ε_r is the low-frequency dielectric constant (static) of the solvent, ε_0 is the dielectric constant (permittivity) of vacuum, T is temperature, k_B is the Boltzmann constant and z_i is the charge of ion i. Thus, the Debye length scales inversely with the square root of bulk ion density (concentration). Within the mean-field Poisson–Boltzmann model, a high concentration of ions leads to screening of an electrostatic potential over short distances [43, 44]. For example, in a solution of NaCl in H_2O (25 °C) and $c = 10^{-3}$, M λ_D is 9.6 nm, and $\lambda_D = 0.96$ nm if $c = 10^{-1}$ M (nearly equivalent to the diameter of only 4 H_2O molecules). At highly concentrated solutions, the Debye–Hückel and Poisson–Boltzmann derived models are not applicable on carbon activated with $ZnCl_2$ at different conditions. With the increase in temperature, the values of λ_D decreases non-linearly causing some increase of conductivity. In addition, the effective diameter of ion [45, 46] decreases with the increase of the cell potential. The differential capacitance C for real geometrical surface with some non-homogeneity can be expressed as:

$$C = C_{GC}(E)\tilde{R}(\kappa, E) \tag{2}$$

where the $C_{GC}(E)$ is the Gouy–Chapman capacitance for an ideally flat surface and $\tilde{R}(\kappa, E)$ is the potential dependent roughness function [44–46]. The $C_{GC}(E)$ is given as:

$$C_{GC}(E) = \frac{\varepsilon \kappa_{eff}(E)}{4\pi}; \tag{3}$$

where the effective diffuse layer thickness $\kappa_{eff}(E)$ is given as:

$$\kappa_{eff}(E) = \kappa \cos\left(\frac{eE}{k_B T} \right), \tag{4}$$

and ε is the dielectric constant of the electrolyte layer, κ is the Gouy length (i.e. the inverse of Debye length), e is the elementary charge and where rational potential $E = E_x - E_{\sigma=0}$, and $E_{\sigma=0}$ is the zero-charge potential and E_x is the measured potential [45, 46].

Thus, the increase of cell potential can be expressed as a nearly linear increase of capacitance, observed for $LiClO_4$, $NaBF_4$, $LiPF_6$, etc. solutions in acetonitrile, ethylene carbonate + propylene carbonate mixtures, etc. [16, 36, 42, 47]. For an ideally flat electrode, $\tilde{R}(\kappa, E) = 1$, and we have

the traditional Grahame results [44–47]. For geometrically rough electrodes, $\tilde{R}(\kappa, E) > 1$.

For ionic liquid electrode interface, Kornyshev et al. have worked out many sophisticated models [48–50]; however, there is no consensus established yet.

Different carbon materials are used in order to prepare the hierarchically micro–mesoporous electrodes for EDLC [6, 8, 51–56]. Organic materials and bioorganic waste materials are quite often being used to prepare cost-effective carbon materials [51, 56–58], but carbide-derived carbons (CDC) have a unique micro–mesoporous hierarchical structure with a narrow pore size distribution, a possibility to fine-tune the pore size and pore volume ratio, and also they have high electrical conductivity [6, 8, 14, 15, 59]. These properties make the CDC materials especially promising for extremely high energy storage/power generation applications [6, 8–10, 13–15]. However, the CDC-based EDLCs are expensive and therefore these materials are very good mainly for detailed fundamental analysis [57–60].

Activated carbon materials are widely studied for several other energy storage applications. In order to improve the specific surface area and average pore size of non-CDC carbon materials, they are often activated by gas-phase (CO_2 and H_2O) or solid-phase ($ZnCl_2$ and/or NaOH or KOH) activation or even combined methods [51, 53, 56–58]. Since gas-phase activation enables cleaner production, it is sometimes more favourable than the solid-phase chemical activation [8–10, 13, 14]. Carbon dioxide and H_2O (steam) are the most widespread activating agents due to cost-efficiency and endothermic nature of their reactions with carbons which allows better process control [8, 30, 51, 61]. However, the $ZnCl_2$ or NaOH activation or combined methods generate more mesoporous carbons that are more suitable for ionic liquids-based EDLCs [30, 42, 58, 59, 61, 63]. Román et al. [58] have reported that while CO_2 produces narrow micropores in the carbons and widens them as activation time is increased, steam treatment of carbons yields pores of all the sizes from the early stages of the process and results in wider pore size distribution and more obvious development of mesopores and macropores in the carbon materials [63]. For wide knowledge collection, all the above-mentioned activation methods have been used for activation of GDC, WSDC and PDC raw materials.

In this study, the EDLCs characteristics based on non-aqueous electrolytes and very pure ionic liquids based on two-electrode cells/devices will be discussed. For detailed analysis, four groups of different carbons have been used: D-glucose-derived carbons (GDC) activated with CO_2 at different activation times (from 0 to 12 h), GDC activated with KOH and/or $ZnCl_2$, granulated white sugar-derived carbons (WSDC) activated with $ZnCl_2$ and the Estonian highly decomposed peat, activated with $ZnCl_2$ under variable activation conditions.

The relationship between activation and posttreatment parameters and the electrochemical characteristics of obtained activated carbon materials like limiting capacitance, characteristic relaxation time, ideal polarizability region, limiting power and energy densities, established using cyclic voltammetry, constant current charge/discharge, impedance analysis with fitting data and experimental constant power discharge data will be presented and discussed.

2 Materials and methods

2.1 Synthesis of carbon material

The carbon materials for supercapacitor electrodes were made from different raw materials: D-glucose (GDC), granulated white sugar (WSDC) and highly decomposed Estonian peat (PDC). GDC and WSDC were synthesized by dissolving D-glucose ($\geq 99.5\%$ purity, Sigma-Aldrich) or commercial granulated white sugar, respectively, in 100 ml of ultrapure water (Milli-Q$^+$, 18.2 MΩ cm, Millipore). Resulting 1 M D-glucose and 0.5 M sugar solutions were used as a precursor for the hydrothermal carbonization process which was carried out in a high-pressure reactor (Büchi limbo, vessel volume 285 ml) at 200 or 260 °C for 24 h. The product was cleaned with Milli-Q$^+$ water followed by drying in a vacuum oven (Vaciotem-TV, J.P. Selecta) at 120 °C and 50 mbar. The synthesis procedures have been described in more detail earlier [31, 42, 61]. The peat for PDC was harvested from Möllatsi peatery in Tartu county, Estonia. The as-received dry peat was mixed with water and blended with a blender and then left to dry in an air atmosphere. The blended dried peat was thereafter mixed with $ZnCl_2$ (1:4 mass ratio) and activated like previously mentioned carbon GDC or WSDC materials [31, 42]. The GDC and WSDC were activated using chemical and physical activation; KOH, $ZnCl_2$ or CO_2 was used as the reactant. After activation, all materials were treated with H_2 (purity 99.9999%) at 800 °C for 2 h in order to remove oxygen-containing functional groups from the surface of the porous carbons. All synthesized materials with their abbreviations are given in Table 1.

2.2 Physical characterization of materials

The morphologies of the samples were characterized by scanning electron microscopy (SEM), using the ZEISS EVO MA15 SEM or the FIB-SEM Helios™ Nanolab 600 systems. The surfaces of the carbon samples were sputter-coated with gold or platinum before SEM measurements. X-ray diffraction (XRD) analysis was performed on Bruker D8 diffractometer (Bruker Corporation) with position-sensitive LynxEye detector using Cu$K\alpha$ ($\lambda = 0.154178$ nm) radiation with an angular step 0.01° and counting time 2 s for

Table 1 Synthesis conditions

Carbon material abbreviation	Synthesis conditions
HTC WSDC	Intermediate material (SEM data only) HTC: 0.5 M sucrose 200 °C for 24 h
HTC CO_2	Intermediate material (SEM data only) HTC: 1 M glucose 260 °C for 24 h
GDC	HTC: 1 M glucose 200 °C for 24 h Pyrolyzed at 700 °C for 2 h (Ar atmosphere)
GDC CO_2 12h	HTC: 1 M glucose 260 °C for 24 h Activation: CO_2 900 °C for 12 h
GDC CO_2 8h	HTC: 1 M glucose 260 °C for 24 h Activation: CO_2 900 °C for 8 h
GDC KOH	HTC: 1 M glucose 200 °C for 24 h Activation: HTC:KOH (1:4 mass ratio) 700 °C for 2 h (Ar atmosphere)
GDC KOH+$ZnCl_2$	HTC: 1 M glucose 200 °C for 24 h Activation: HTC:KOH:$ZnCl_2$ (1:2:2 mass ratio) 700 °C for 2 h (Ar atmosphere)
GDC $ZnCl_2$	HTC: 1 M glucose 200 °C for 24 h Activation: HTC:$ZnCl_2$ (1:4 mass ratio) 700 °C for 2 h (Ar atmosphere)
PDC $ZnCl_2$	Direct activation Peat:$ZnCl_2$ (1:4 mass ratio) 700 °C for 2 h (Ar atmosphere)
WSDC $ZnCl_2$	HTC: 0.5 M sucrose 200 °C for 24 h Activation: HTC:$ZnCl_2$ (1:4 mass ratio) 700 °C for 2 h (Ar atmosphere)

each fixed angle measured. Diffraction spectra were recorded at temperature of 25 ± 1 °C. Raman spectra were recorded using a Renishaw inVia micro-Raman spectrometer with Ar laser excitation beam ($\lambda = 514$ nm). The obtained spectra were baseline corrected using 4th-order polynomial and normalized relative to the G-band intensities. Experimental data were fitted with a combination of Lorentzian and Gaussian functions. The lowest fitting error was achieved with a combination of 4 Lorentzian functions (Figs. S1). Raman data analysis was done using OriginPro 2016 software.

The porous structure of the activated carbon materials has been characterized using the low-temperature nitrogen sorption method at the boiling temperature of liquid nitrogen (-195.8 °C) with the 3Flex surface characterization system (Micromeritics, USA). The specific surface area, S_{BET}, has been calculated according to the Brunauer–Emmett–Teller (BET) theory [64]. The total volume of pores, V_{tot}, has been obtained at the conditions near to saturation pressure, $p/p_0 = 0.95$. The pore size distribution plots have been calculated by applying two-dimensional non-local density functional theory for carbon materials with the heterogeneous surface (2D-NLDFT-HS) to the N_2 adsorption isotherm data using the Solution of Adsorption Integral Equation Using Splines (SAIEUS) (Micromeritics, USA) software [65]. Compared to previously introduced modifications of NLDFT, the 2D-NLDFT-HS model takes into account the surface curvature of graphitic layers and the energetic heterogeneity of carbon (influenced by geometric roughness) surfaces caused by chemical composition, impurities, and surface chemical groups [66]. Thus, applied

2D-NLDFT-HS methods yield the pore size distributions with a smoother and more realistic shape for different amorphous micro–mesoporous carbon materials.

2.3 Electrode preparation, cell assembly and electrochemical characterization of materials

Carbon electrodes were prepared from different synthesized carbon materials (94 wt%) adding a 6 wt% of binder (prepared from polytetrafluoroethylene, PTFE, 60% dispersion in H_2O, Sigma-Aldrich). The mixture of the synthesized carbon material and binder was laminated and roll-pressed (HS-160 N, Hohsen Corporation, Japan) to form an elastic layer of the carbon electrodes with a thickness of 105 ± 5 μm. After drying under vacuum, for better electrochemical (homogeneous) polarization of carbon layers, the pure Al layer (2 μm) was deposited onto one side of the carbon material using a magnetron sputtering method. Standard two-electrode test cells (aluminium, HS Test Cell, Hohsen Corporation) were assembled using two identical carbon electrodes (geometric area of 2.0 cm^2) and 25-μm thick TF4425 (Nippon Kodoshi) separator sheet. 1-ethyl-3-methylimidazolium tetrafluoroborate (EtMeImBF$_4$, Sigma-Aldrich, for electrochemistry, $\geq 99.0\%$, $H_2O < 200$ ppm) or 1 M Et$_3$MeNBF$_4$ (Stella Chemifa) solution in acetonitrile (AN, $H_2O < 20$ ppm, Sigma-Aldrich) was used as an electrolyte. The cells were completed inside a glove box (Labmaster sp, MBraun, O_2 and H_2O concentrations lower than

0.1 ppm). All electrochemical experiments were carried out at temperature $T = 20 \pm 1$ °C.

The electrochemical characteristics of EDLCs were established by the electrochemical impedance spectroscopy (EIS), cyclic voltammetry (CV), constant current charge/discharge (CC) and the constant power (CP) discharge methods. Impedance spectra (over ac frequency range from 1 mHz to 300 kHz with perturbation of 5 mV), CV and CC curves were recorded using a frequency response analyser 1252A and potentiostat SI1287 (Solartron, UK). The CP tests were carried out on a BT2000 testing system (Arbin Instruments, USA). ZView 3.5d was used for equivalent circuit fitting and LIN-KK for Kramers–Kronig analysis.

3 Results and discussion

3.1 Physical characterization of activated carbon material

SEM data, given in Figs. 1 and 2, show the surface structure of precursor materials (HTC CO_2, GDC and PDC) and their chemically activated post-products. It is clearly visible that surface morphology strongly depends on the raw material and chemical activation conditions (CO_2, KOH; $ZnCl_2$, and/or KOH + $ZnCl_2$). Non-activated precursor materials (HTC CO_2, HTC WSDC and GDC) and $ZnCl_2$ activated materials consist of spherical-shape particles with some interconnection between spheres. The microspheres generated during hydrothermal carbonization are rather characteristic of the

precursor and method used [30, 31, 63, 67]. Average (arithmetic mean) diameter, standard deviation (SD) and median diameter values of spherical particles are presented in Figs. 1 and 2, established using fitting program Adobe Acrobat X Pro. Most of the materials that were statistically analysed have sphere diameter values from 0.85 to 1.11 μm with the exception of WSDC materials that have particle diameter around 3 μm (Fig. 2). The KOH and KOH + $ZnCl_2$ mixture activated powders have a very complicated structure, especially when high amounts of KOH have been added to raw hydrothermal carbon mass (Fig. 1). On the other hand, the $ZnCl_2$ activation (GDC $ZnCl_2$, WSDC $ZnCl_2$) seems to have very little or no effect on the surface morphology of particle (Fig. 1). In general, there are porous layers with a random distribution of surface defects presented at the chemically activated GDC surfaces. Very non-homogenous particles size dimension distribution has been calculated for non-activated peat and PDC $ZnCl_2$ powder. Both powders consist of particles that have a very complicated non-spherical shape.

3.2 X-ray diffraction and Raman spectroscopy data

In order to further characterize the possible graphitization of porous carbons, a Raman spectroscopy analysis was carried out and the results are shown in Fig. S2. The first-order region of Raman spectra shows two characteristic peaks for amorphous carbon materials: one at Raman shift ~ 1334 cm^{-1} (D-peak) and second at ~ 1594 cm^{-1} (G-peak) [30, 42, 67–70]. The G-band is assigned to the doubly degenerate Raman-active E_{2g} in-plane vibration mode
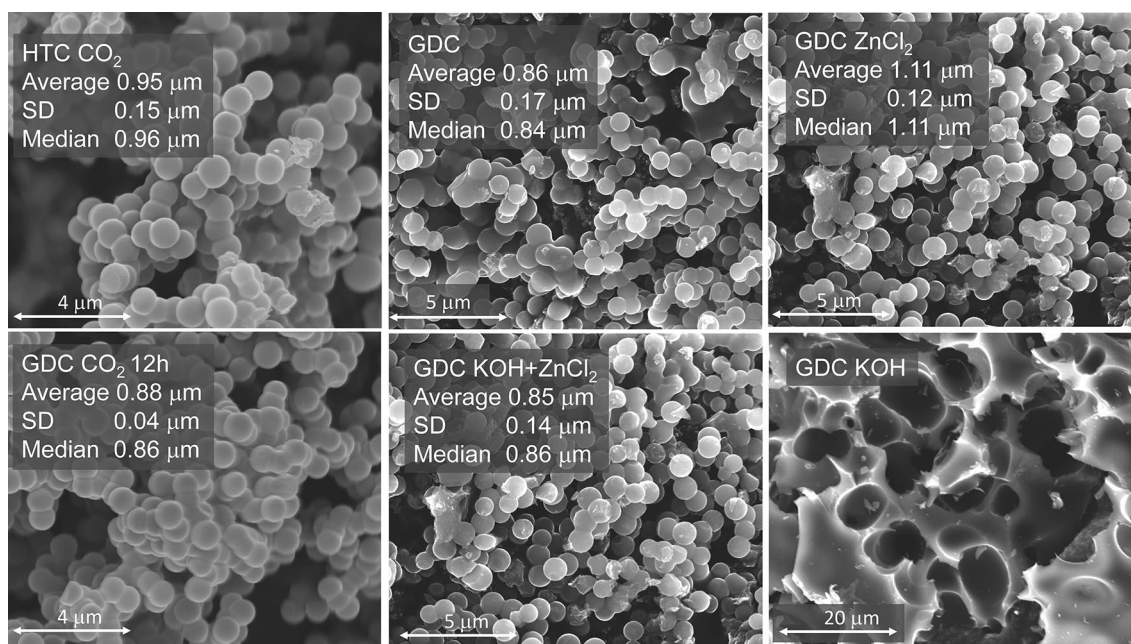

Fig. 1 SEM images for hydrothermal carbons and carbon materials from D-glucose (details noted in the figure)

which is attributed to the in-plane stretching motion of sp^2 carbon atom pairs. The presence of G-band indicates that the sample contains sp^2 carbon networks. In contrary, the D-peak originates from defect-induced Raman features such as A_{1g} symmetry. This peak reflects the presence of amorphous areas in carbon particles. The integrated D-band and G-band intensity ratio I_D/I_G is widely used to characterize the defect quantity in graphitic materials [42, 68–72]. As can be seen in Fig. S2, the far-field Raman spectra for all materials exhibited similar Raman peak activities. The values of I_D/I_G (about 0.9) demonstrate low graphitization degree of the zinc chloride-activated carbon material, whereas CO_2-activated materials show slightly higher I_D/I_G (about 1.05) which indicates a somewhat lower disorder in the particles. Surprisingly, all the materials show remarkable similarities in the 2D region (2600–3200 cm^{-1}) indicating that the stacking order of graphite planes are not tied to the method of activation [72].

As depicted in Fig. S2, the XRD patterns of the synthesized carbon material exhibit very weak diffraction peaks corresponding to the graphite (hexagonal symmetry, space group P6$_3$/mmc) 002 peak at $2\theta \sim 25°$ and 100/101 peak at $2\theta \sim 43°$. No other peaks are found in the XRD patterns. All sugar-derived carbon materials have nearly similar shape diffractograms, where the two observed peaks are characteristic of mainly amorphous carbon materials [13, 41, 42, 73–75]. However, the PDC material shows slightly lower intensities, which may be caused by differences in material surface roughness and other external causes. Thus, Raman spectroscopy and XRD data show that the carbon materials are primarily amorphous.

3.3 Gas adsorption data analysis

N_2 adsorption isotherms with the 2D-NLDFT-HS model fits are presented in Fig. 3a and b. The shape of an isotherm is strongly influenced by the choice of raw material, physical and chemical conditions of carbon synthesis, i.e. by the crystallographic structure and density of defects in the carbon electrode and on the powder surface (Figs. 1, 2 and S2). For GDC materials, the limiting adsorption value (a plateau in isotherms) is reached at low relative pressures, p/p_0, which is characteristic of materials without a substantial amount of mesopores. Chemically activated carbons GDC KOH, GDC $ZnCl_2$, WSDC $ZnCl_2$ and PDC $ZnCl_2$ exhibit gradually increasing amounts of adsorbed N_2 with the increase in logarithmically scaled p/p_0, which is characteristic of materials having some mesoporosity in addition to the micropores. PDC $ZnCl_2$ exhibits some hysteresis between the adsorption and desorption isotherms, which is characteristic of micro–mesoporous materials.

The highest amount of N_2 has been adsorbed by WSDC $ZnCl_2$, GDC KOH and GDC $ZnCl_2$, having a very high specific surface area and micro–mesopore volume values (Table 2). GDC, without chemical activation, exhibits lowest specific surface area, $S_{BET} < 540$ m^2 g^{-1}

Fig. 2 SEM images for hydrothermal carbons and carbon materials from granulated white sugar and peat (details noted in the figure)
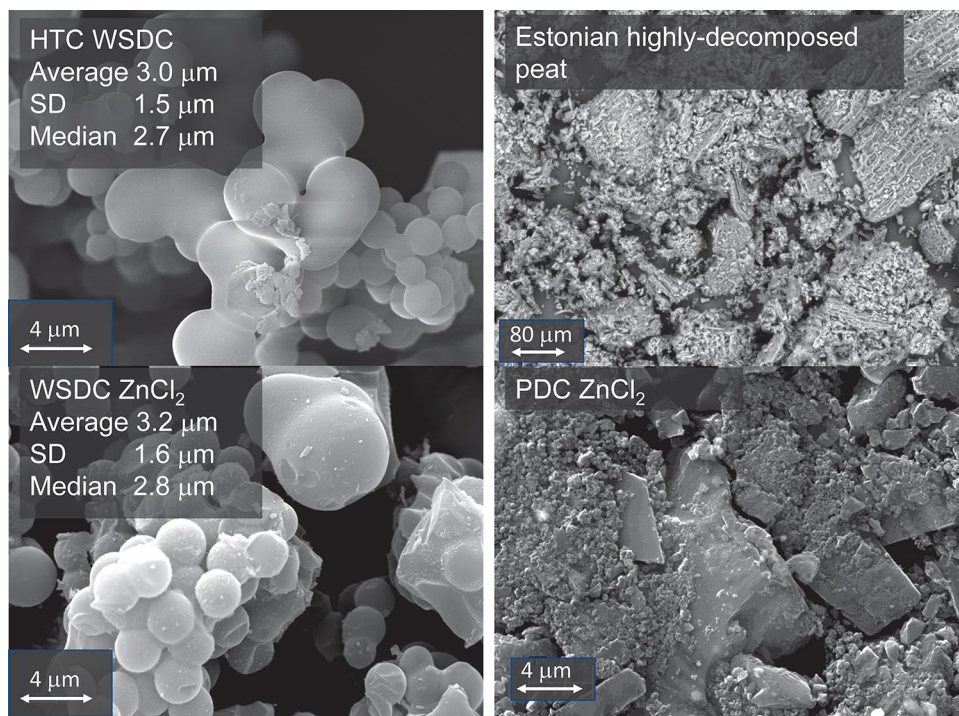
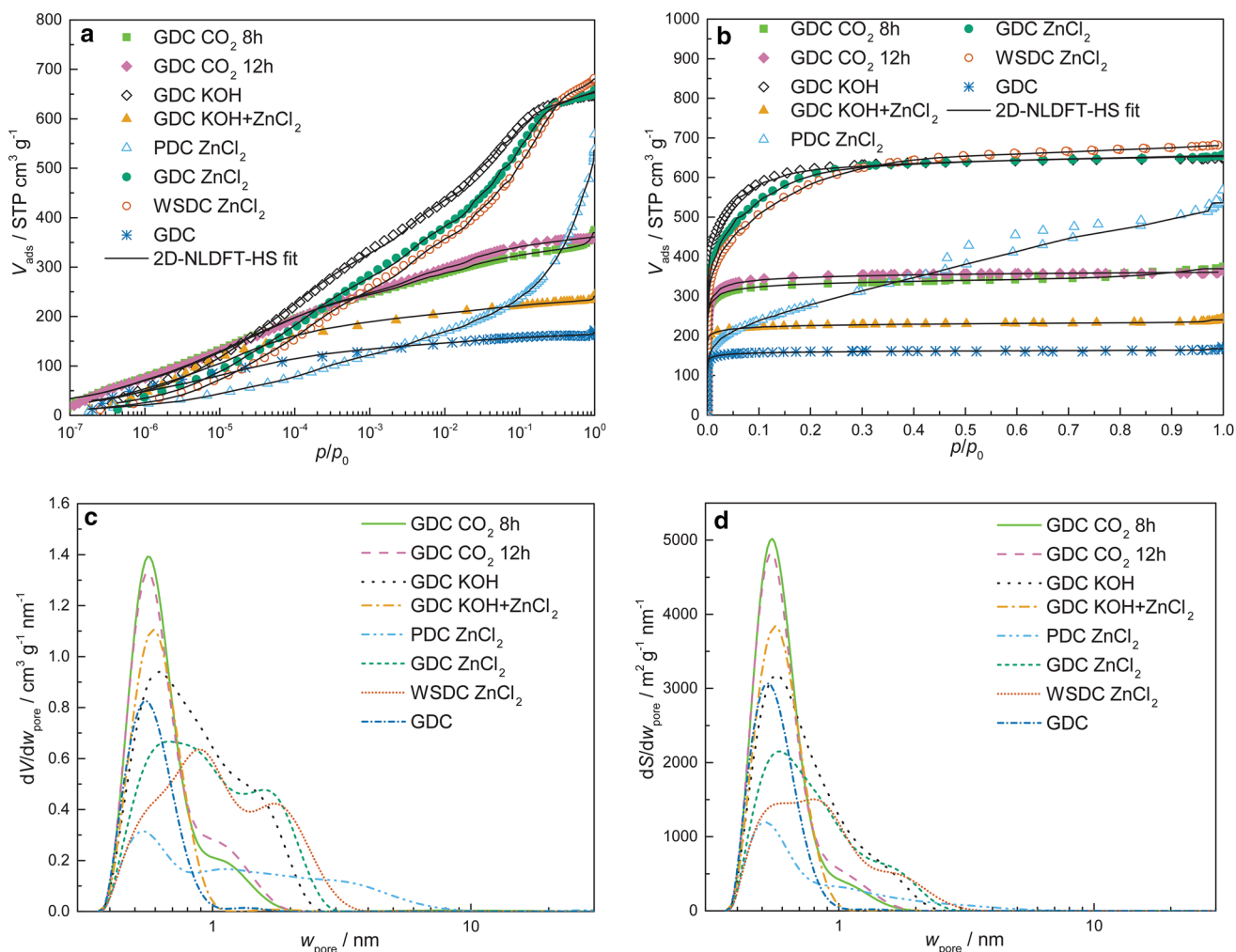**Fig. 3** N$_2$ adsorption and desorption isotherms presented in linear (**a**), and logarithmic (**b**) relative pressure p/p_0 scale, pore size distributions versus differential pore volume plots (**c**) and differential specific surface area (**d**) versus pore widths plots calculated according to the 2D-NLDFT-HS model using SAIEUS software from N$_2$ adsorption data (fits calculated by 2D-NLDFT-HS model are presented as dashed lines in **a** and **b**)

Table 2 Sorption analysis data

Carbon material	S_{BET} (m^2 g^{-1})	V_{tot} (cm^3 g^{-1})	S_{DFT} (m^2 g^{-1})	V_{DFT} (cm^3 g^{-1})
GDC CO$_2$ 12 h	1240	0.56	1530	0.53
GDC CO$_2$ 8 h	1160	0.57	1510	0.55
GDC KOH	2150	1.00	1990	0.93
GDC KOH + ZnCl$_2$	750	0.37	1120	0.36
GDC ZnCl$_2$	2150	1.01	1740	0.92
PDC ZnCl$_2$	1000	0.83	840	0.78
WSDC ZnCl$_2$	2110	1.05	1600	0.96
GDC	540	0.26	840	0.26

S_{BET}-specific surface area is calculated according to the BET theory, V_{tot} total volume of pores is calculated from the adsorbed amount near the saturation pressure, S_{DFT}- and V_{DFT}-specific surface area and total pore volume, respectively, are calculated with the 2D-NLDFT-HS model using the SAIEUS software [65]

and $S_{DFT} < 850$ m^2 g^{-1}, and total pore volume, V_{tot} and $V_{DFT} < 0.26$ cm^3 g^{-1}, of investigated carbon materials.

The pore size distributions data, presented in Fig. 3c and d, are very different depending on the synthesis conditions of carbon powder. For GDC and WSDC powders, two clearly visible maxima in the microporous region are observed, one at pore widths, w_{pore}, of 0.6–0.7 nm (so-called ultramicropore region) and second at 1.5 nm in the case of activating GDC with KOH or ZnCl$_2$ and at 1.0 nm in the case of GDC CO$_2$ activation (all in the micropore region) (Fig. 3c). In the case of GDCs activated with CO$_2$, the positions of pore size distribution maxima are practically independent of CO$_2$ activation time applied and only the amount of pores (expressed as specific surface area and total pore volume) changes with the duration of the CO$_2$ activation [61]. For GDCs and WSDCs activated with ZnCl$_2$ or KOH, there is a noticeable dependence of the second pore size distribution peak position on the chemical composition of activating agent and synthesis conditions used. In addition, the pore volume increases noticeably for pores with w_{pore} from 0.9 to 2.0 nm, if activation with KOH or ZnCl$_2$ is used instead of pyrolysis and CO$_2$

activation. However, almost no mesopores ($w_{pore} > 2.0$ nm) have been formed during the chemical activation of GDC and WSDC. PDC activated with ZnCl$_2$ exhibits a considerable amount of mesopores ($w_{pore} > 2.0$ nm), indicating that the peat-derived carbon can be tuned further for high energy and power density supercapacitor applications. Based on the analysis of gas adsorption data, the electrochemical characteristics can be tunable in a very wide range.

3.4 Cyclic voltammetry data

CV data have been measured at different potential scan rates (v) from 10 mV s^{-1} to 200 mV s^{-1} and are given as the capacitance versus cell potential ($C, \Delta E$) curves in Figs. 4a–d. The current density, j (calculated using the flat cross-section geometric surface area), measured at fixed potential scan rate has been used for calculation of the medium capacitance values according to Eq. (5):
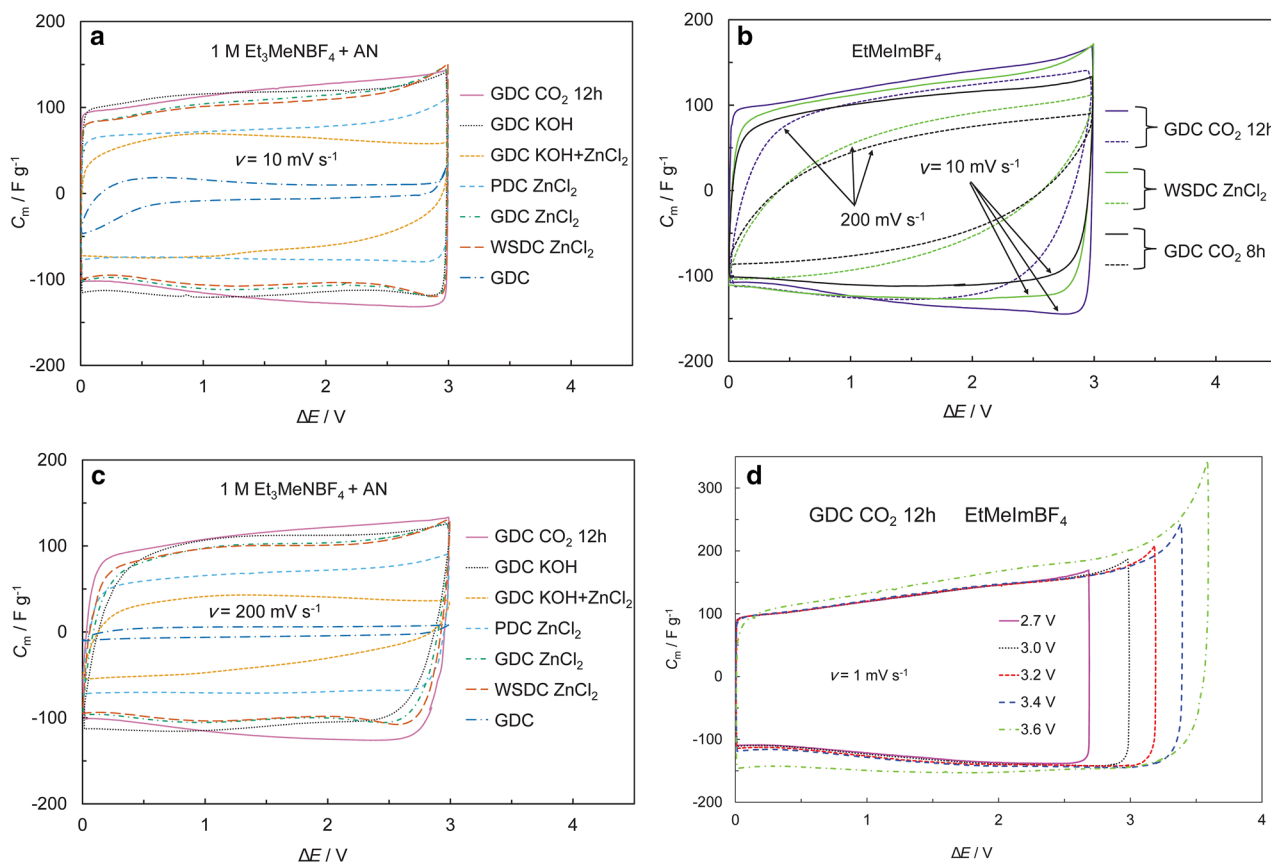
$$C = jv^{-1} \tag{5}$$

Fig. 4 Cyclic voltammetry curves expressed as specific capacitance versus cell potential dependencies ($C_m, \Delta E$) for the EDLCs based on the different carbon materials in Et$_3$MeNBF$_4$ in AN (**a**, **c**) and EtMeImBF$_4$ ionic liquid (**b**, **d**) (noted in the figure) at cell potential scan rates $v = 10$ mV s^{-1} (**a**, **b**) and $v = 200$ mV s^{-1} (**c**) (noted in figure) within the cell potential range from 0 to 3.0 V. $C_m, \Delta E$ dependencies for CDC CO$_2$ 12 h in EtMeImBF$_4$ at $v = 1$ mV s^{-1} for different potential ranges (**d**)

where j is the current density (per geometrical surface area of an electrode, assuming $\tilde{R}(\kappa, E) = 1$), ν is the potential scan rate and C is the cell capacitance. Equation 5 is correct if the capacitance C does not depend on the potential applied [$C \neq f(\Delta E)$] and the series resistance of the system $R_s \to 0$; thus, the current response is essentially equal to that of a pure capacitor [4, 8, 43, 75–78]. In a symmetrical two-electrode system, the specific capacitance, C_m (F g^{-1}), for one activated carbon electrode can be obtained as follows:

$$C_m = \frac{2C}{m}, \tag{6}$$

where m is the weight in g cm^{-2} per one activated carbon electrode, assumed that the positively and negatively charged electrodes have the same capacitance at fixed cell potential ΔE. Data in Fig. 4 show the nearly ideal quasi-rectangular $C, \Delta E$ curves if $v < 100$ mV s^{-1}. A small increase in capacitance at high E can be explained by the decrease in the effective liner dimension of ions with cell potential (Eqs. 2–4). However, for non-activated or less activated GDC (activation with KOH + ZnCl$_2$ and 8-h activation with CO$_2$), there is a noticeable dependency of C (at fixed ΔE) even at very low potential scan rates, explained by the absence of mesopores (as well as larger micropores, Figs. 3c and d) in the carbon particles, established by gas adsorption analysis methods. It is interesting to stress that noticeably higher scan rates can be applied for analysis of chemically activated GDC with KOH or ZnCl$_2$ and WSDC ZnCl$_2$, i.e. for materials with highly expressed amounts of larger micropores ($w_{pore} > 1.0$ nm) as well as some mesopores in particles (data in Fig. 4a–c). It should be stressed that GDC KOH and WSDC ZnCl$_2$ demonstrated very high capacitance values even at $v = 1$ V s^{-1} (not shown in Figures for shortness). Even

higher capacitance values have been calculated for heavily micro–mesoporous GDC CO$_2$ 12-h carbon materials-based EDLCs. PDC materials show moderate capacitance values at v from 10 to 200 mV s^{-1}. Thus, future chemical activation procedures of PDC ZnCl$_2$ powders are inevitable for materials for high energy density EDLCs. CV data show that materials with heavily different micro–mesoporous structure have very widely spread electrochemical behaviour in 1 M Et$_3$MeNBF$_4$ in AN solution.

$C, \Delta E$ plots for EtMeImBF$_4$ ionic liquid electrolyte and GDC, chemically activated GDC and WSDC ZnCl$_2$ electrodes-based EDLCs, are very variable. Data in Fig. 4b show that due to the higher viscosity of EtMeImBF$_4$, the dependence of capacitance on v is more noticeable, when $v > 50$ mV s^{-1}. Higher potential scan rates can be applied for GDC CO$_2$ 12-h GDC KOH and WSDC ZnCl$_2$ completed EDLCs. Data in Fig. 4d show very high discharge capacitance values for GDC CO$_2$ 12 h at cell potential $\Delta E \leq 3.2$ V.

The integrated capacitance values have been calculated over the cell potential range ΔE from 0 to 3.0 V, using the total charge q values obtained according to Eq. (7):

$$q = \int_{\Delta E_1}^{\Delta E_2} j(\Delta E) dt \equiv \int_{\Delta E_1}^{\Delta E_2} j(\Delta E) \frac{d(\Delta E)}{v}. \tag{7}$$

Integrated capacitance values are given in Table 3.

3.5 Constant current charge/discharge data

Constant current charge/discharge (CC) data, given in Fig. 5a, b show, that only at moderate discharge (or charge) current densities, there are linear plots and the charge and discharge curves are symmetrical. For many systems, there

Table 3 Calculated capacitance and characteristic time constant values

Carbon material	Electrolyte	C_{CV} (F g^{-1})	C_{CC} (F g^{-1})	C_s (F g^{-1})	τ_{char} (s)
GDC CO$_2$ 12 h	Et$_3$MeNBF$_4$ in AN	125	N/A	126	0.42
GDC CO$_2$ 8 h	Et$_3$MeNBF$_4$ in AN	108	N/A	102	N/A
GDC KOH	Et$_3$MeNBF$_4$ in AN	131	136	134	0.84
GDC KOH + ZnCl$_2$	Et$_3$MeNBF$_4$ in AN	77	57	79	1.06
GDC ZnCl$_2$	Et$_3$MeNBF$_4$ in AN	112	108	118	0.84
PDC ZnCl$_2$	Et$_3$MeNBF$_4$ in AN	80	77	83	0.33
WSDC ZnCl$_2$	Et$_3$MeNBF$_4$ in AN	110	109	121	0.53
GDC	Et$_3$MeNBF$_4$ in AN	19	5	6	0.21
WSDC ZnCl$_2$	IL (EtMeImBF$_4$)	134	136	141	4.21
GDC CO$_2$ 12 h	IL (EtMeImBF$_4$)	125	N/A	144	1.68
GDC CO$_2$ 8 h	IL (EtMeImBF$_4$)	117	N/A	114	4.21

C_{CV}-specific capacitance is calculated from CV curves within the cell potential range from 0 to 3.0 V using the integrated charge q obtained according to Eq. 7 and at a v of 1 mV s^{-1}; C_{CC} average-specific capacitance is calculated from CC curves within the cell potential range from 1.5 to 3.0 V, according to Eq. 8; C_s-specific series capacitance is calculated from electrochemical impedance data at cell potential $\Delta E = 3.0$ V, τ_{char} characteristic time constant is calculated from C'' vs. log (f) maximum frequency values (C'' is imaginary part of complex capacitance) [8, 61]
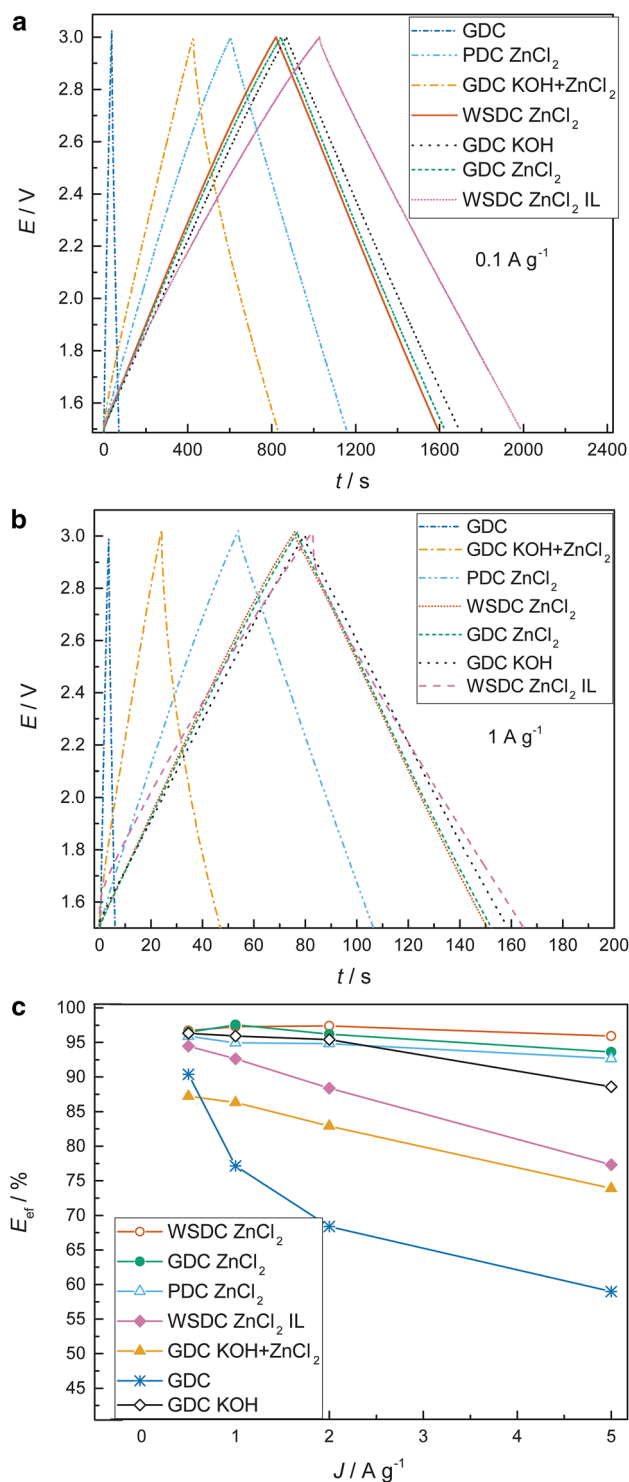
Fig. 5 Constant current charge/discharge cycles at current density $j = 0.1$ A g^{-1} (**a**) and $j = 1$ A g^{-1} (**b**) and integrated energy efficiency (discharge/charge energy) versus j graphs (**c**) for the EDLCs based on the different carbon material in Et$_3$MeNBF$_4$ in AN and EtMeImBF$_4$ ionic liquid (noted in the figure)

is no visible iR-drop region, explained by the low series resistance of materials and the resistance of the electrolyte layer engaged into the porous electrode matrix. At higher discharge current densities ($j > 5$ A g^{-1}), the CC plots are non-linear (not shown for shortness). Thus, for correct quantitative analysis, these data have been integrated and the integral capacitance values have been obtained according to the Eq. (8)

$$C = \frac{\int_{\Delta E_1}^{\Delta E_2} j \mathrm{d}t}{\mathrm{d}(\Delta E)} \tag{8}$$

where j is the current density, dt is the change in time and ΔE is the cell potential. Capacitance values are collected in Table 3.

The energetic efficiency ($E_{\mathrm{ef}} = E_{\mathrm{out}}/E_{\mathrm{in}}$) values have been calculated from integrated energy density values, where E_{out} is the energy delivered during the discharging and E_{in} is the energy accumulated during the charging step [8, 9].

Very high energy efficiency values (higher than 95%) have been established within moderate cell potential region (from 3.0 to 1.5 V). At higher cell charging rates, the energy efficiency starts to decrease. Data in Fig. 5c show that very high discharge/charge current densities can be applied for EDLCs, if the electrodes have a substantial amount of mesoporosity, indicating that high power density devices can be completed. EDLC material lacking mesopores (GDC, GDC KOH + ZnCl$_2$) exhibit much lower energy efficiency values (< 90%), especially higher charging/discharging rates.

Up to 20% longer charging/discharging current pulses have to be applied for ionic liquid-based EDLCs to have high energy efficiency (93%) values during EDLC charging/discharging. It is mainly caused by the lower electrical conductivity (i.e. lower mass-transfer rate) as well as higher viscosity of EtMeImBF$_4$ ionic liquid in micro–mesoporous electrode matrix. Therefore, less viscous room temperature ionic liquids should be used for the preparation of EDLCs with higher energy efficiency.

3.6 Impedance data

Nyquist plots, i.e. impedance imaginary part $-Z''$ versus real part Z' dependences analysis, presented in Fig. 6a–d show that the shape of Nyquist and Bode plots measured for GDC, chemically activated GDC, WSDC ZnCl$_2$ and PDC powders-based two-electrode cells depends noticeably on the carbon powder characteristics. For 1 M Et$_3$MeNBF$_4$ solution in acetonitrile, Nyquist plots have been measured within the range of ac frequency from 1 mHz to 300 kHz and at fixed cell potentials from 0 to 3.2 V for different materials. At fixed $\Delta E = 2.7$ V, the shape of Nyquist plots is very variable within the high and medium (so-called micro–mesopore) ac
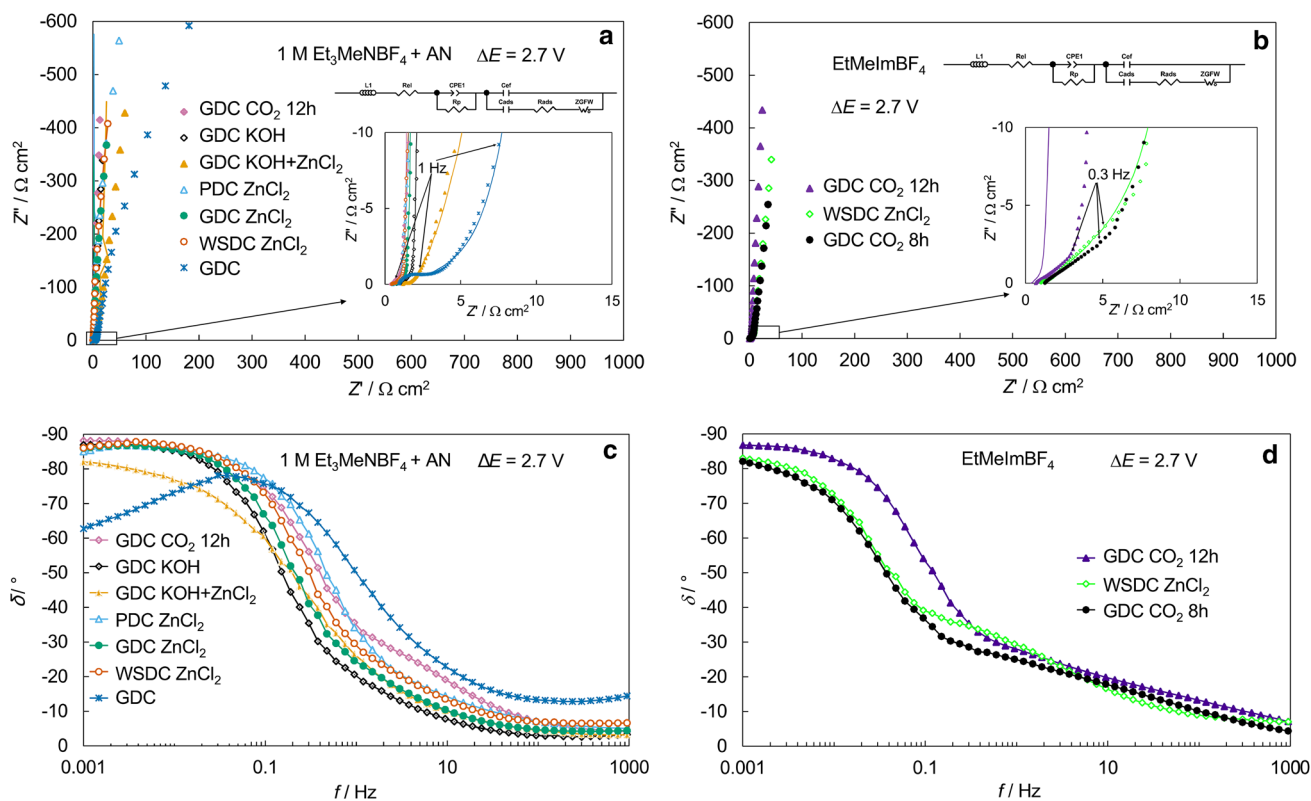
Fig. 6 Impedance complex plane (Nyquist) plots dependencies for the EDLCs based on the different carbon material (noted in the figure) in Et_3MeNBF_4 in AN (**a**) and $EtMeImBF_4$ ionic liquid (**b**), phase angle versus ac frequency plots dependencies for the EDLCs based on the different carbon material (noted in the figure) in Et_3MeNBF_4 in AN (**c**) and $EtMeImBF_4$ ionic liquid (**d**)

frequency region. Thus, the high-frequency series resistance very noticeably depends on the macro/mesoporous structure of the powders used for preparation of the electrodes. Within medium frequency region, there is a nearly linear region in Nyquist plots, with slope value bit lower than $-45°$ [60, 61]. This region is called the porous (micro–mesoporous) area and is characteristic of finite-length mass-transfer processes in mesopores. At very low ac frequencies, the finite-length adsorption effects prevail [8, 30, 31, 42, 60, 61].

It should be noted that the shape of the $-Z''$, Z' plots are similar for all the CO_2-activated carbons, showing no significant influence of the activation duration on the Nyquist plots within ideal polarizability region. This result is in an agreement with the gas adsorption, XRD as well as Raman data, where no influence of CO_2 treatment duration on the pore size distribution and crystallographic structure has been found (Figs. 1, S2 and 3). The gas-phase N_2 adsorption, SEM–EDX, HR-TEM (SAED, EELS) and XPS (not discussed for shortness) data for chemically activated GDC confirm that the difference in chemical surface composition for H_2-treated materials is negligible. For chemically activated GDC and WSDC $ZnCl_2$ and PDC $ZnCl_2$, very complicated Nyquist plots have been measured if $\Delta E > 3.2$ V.

EIS data shown in Fig. 6a and b were fitted with the same equivalent circuit (EC) (shown in the graph) to compare different materials in detail. Prior to fitting, Kramers–Kronig analysis was carried out on EIS data to determine the suitable error-free frequency range. The best fit was obtained with a circuit model that consisted of eight elements in total [61]. In the EC, L is taking into account the high-frequency wire inductance, R_{el} is regarded as a total high-frequency series resistance, C_{ef} is a "true" interfacial capacitance (without adsorption effects) and C_{ads} is adsorption capacitance (Fig. 6a, b) corresponding to the slow adsorption processes in parallel with adsorption resistance, R_{ads} (Fig. 6a, b). The generalized finite Warburg element with a transmission boundary condition $Z_{GFW} = R_D \text{ctnh}[(jT\omega)^{aW}]/(jT\omega)^{aW}$ describes the mass-transport processes in EDLC. The constant phase element (CPE) in EDLC is used to describe the dissipative capacitance at the rough solid–liquid interfaces [62]. Resistance, R_D, what is in parallel with CPE, describes the high-frequency behaviour. All EDLCs except GDC CO_2 8 h IL fitting resulted in conclusive data which are shown in Table 4 with corresponding fitting errors. From Fig. 6a, b and Table 4, it can be seen that EC is more accurate for AN-based electrolyte EDLC than for IL-based electrolyte

Table 4 Fitting results

Carbon material and electrolyte	$R_p/\Omega\ cm^2$	$C_{ef}/\mu F\ cm^{-2}$	$C_{ads}/F\ cm^{-2}$	$R_{ads}/\Omega\ cm^2$	$Z_{GFE}\ R/\Omega\ cm^2$	$Z_{GFE}\ T/s$
GDC CO_2 12 h AN	1.181 ± 0.048	263 ± 23	0.3743 ± 0.0015	0.0704 ± 0.0031	0.88 ± 0.35	163.7 ± 0.20
WSDC $ZnCl_2$ AN	1.39 ± 0.13	217 ± 20	0.3902 ± 0.0018	0.111 ± 0.074	0.49 ± 0.25	165 ± 0.03
PDC $ZnCl_2$ AN	3.5 ± 1.9	219 ± 51	0.2762 ± 0.0016	0.05706 ± 0.0097	1.12 ± 0.37	165 ± 0.07
GDC $ZnCl_2$ AN	1.72 ± 0.25	331 ± 2.5	0.4667 ± 0.0030	0.1746 ± 0.0078	91 ± 34	196 ± 25
GDC KOH AN	1.29 ± 0.10	19.19 ± 0.92	0.4836 ± 0.0024	0.3810 ± 0.0088	0.43 ± 0.20	164.9 ± 0.004
GDC KOH+$ZnCl_2$ AN	$12 \pm N/A$	11.6 ± 0.7	0.285 ± 0.004	0.488 ± 0.012	237 ± 16	196.7 ± 6.5
GDC AN	5.6 ± 1.2	53 ± 21	0.0600 ± 0.0062	0.49 ± 0.13	5440 ± 540	485 ± 20
GDC CO_2 12 h IL	0.878 ± 0.045	273 ± 19	0.435 ± 0.025	0.0762 ± 0.0026	92 ± 33	339 ± 43
WSDC $ZnCl_2$ IL	14.07 ± 0.94	103 ± 10	0.4869 ± 0.0045	0.289 ± 0.015	0.46 ± 0.21	165.6 ± 0.023

In the EC, L is high-frequency wire inductance, C_{ef} is "true" interfacial capacitance (without adsorption effects), C_{ads} is adsorption capacitance and R_{ads} is adsorption resistance. The Z_{GFW} generalized finite Warburg element where R is diffusion resistance and T is time constant. R_p is the parallel resistance, which describes the high-frequency behaviour

EDLC. Our fitting results revealed that the C_{ads} values are more than three orders greater than C_{ef} values. This means that the $C_s(f \rightarrow 0)$ is mainly caused by the slow adsorption steps of electrolytic ions onto/into the porous electrode surface. It also seems that R_{ads} values are greater for material with lower mesoporosity due to having less developed mass-transport network.

For more correct analysis, the series capacitance C_s versus $\log(f)$ and parallel capacitance C_p versus $\log(f)$ plots have been calculated at fixed cell potentials and are given in Fig. 7a–d. For many two-electrode systems, long linear plateaus have been observed. At $f = 1$ mHz, C_p/C_s versus $\log(f)$ plots overlap, indicating that the limiting ideal capacitance values (free from faradic contribution) have been established.
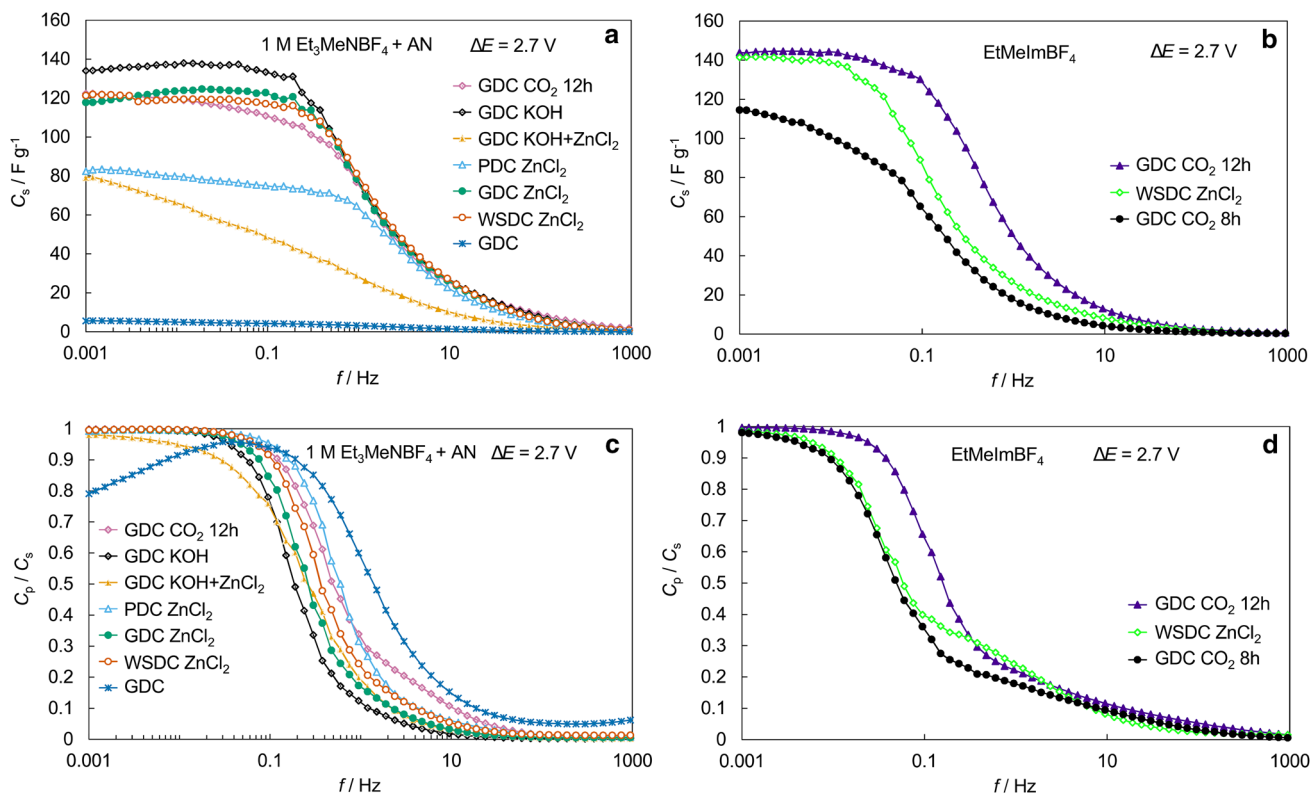

Fig. 7 Specific series capacitance versus ac frequency dependencies for the EDLCs based on the different carbon material (noted in the figure) in Et_3MeNBF_4 in AN (**a**) and $EtMeImBF_4$ ionic liquid (**b**), series capacitance/parallel capacitance versus ac frequency dependencies for the EDLCs based on the different carbon material in Et_3MeNBF_4 in AN (**c**) and $EtMeImBF_4$ ionic liquid (**d**)

Calculated C_p (as well as C_s) values show a bit higher capacitance values compared to those obtained by CC and CV methods but are showing the same increasing dependency from non-activated GDC to KOH-activated GDC. High C_s and C_p values at low f and high electrode potentials for GDC CO$_2$ 12 h ($C_s = 143$ F g^{-1}; $C_p = 144$ F g^{-1}) and WSDC ZnCl$_2$ IL ($C_s = 141$ F g^{-1}; $C_p = 139$ F g^{-1}) have been calculated for Et$_3$MeNBF$_4$ electrolyte. For 1 M Et$_3$MeNBF$_4$ solution in AN, approximately 10–15% smaller capacitance values have been calculated.

It should be noted that the characteristic relaxation frequency values f_{char} (frequency value, where the imaginary part of the capacitance is highest), depend heavily on the carbon material under study (Fig. 8a, b; Table 3). Very short τ_{char} values [$\tau_{char} = (2\pi f_{char})^{-1}$] have been calculated for GDC CO$_2$ 12 h ($\tau_{char} = 0.42$ s) and WSDC ZnCl$_2$ ($\tau_{char} = 0.52$ s). Only somewhat longer τ_{char} values have been calculated for GDC KOH + ZnCl$_2$ (1.06 s) and GDC ZnCl$_2$ (0.84 s) in AN-based electrolytes.

The very wider region of ideal polarizability has been achieved for EtMeImBF$_4$-based EDLC devices. Noticeable deviations from the linear shape (> 0.98 slope) started only at $\Delta E > 3.2$ V, (Fig. S3) where faradic reactions started.

Data in Fig. 9a show that τ_{char} increases with the specific surface area as well as with the total (and micropore) volume, calculated using gas adsorption data. Thus, τ_{char} can be correlated with the value of accumulated charge density, (calculated by integration of CV curves), adsorbed during the charging/discharging process. Therefore, to a first approximation, τ_{char} is determined by the mass-transfer rate of ions in the porous electrode structure. Within the ideal polarizability region, τ_{char} is not characteristic of the adsorption step (rate) limited processes.

For micro–mesoporous PDC ZnCl$_2$ with moderate specific surface area and pore volume value, very short τ_{char} values (0.33 s) have been established, even somewhat shorter than that for GDC CO$_2$ 12 h (0.42 s). It is interesting that τ_{char} is practically independent of chemical activation conditions of materials applied for GDC KOH or GDC ZnCl$_2$ and GDC CO$_2$ 12-h materials. For GDC KOH or GDC ZnCl$_2$ and WSDC ZnCl$_2$, there is a very strong influence of activation conditions on the τ_{char} values, explained that for WSDC ZnCl$_2$ and GDC KOH or GDC ZnCl$_2$, the ratio of micropores/smaller micropores ($w_{pore} < 1.0$ nm) increases noticeably with activation (in an agreement with data in Fig. 3). As a whole, the materials with the highest C_s values do not
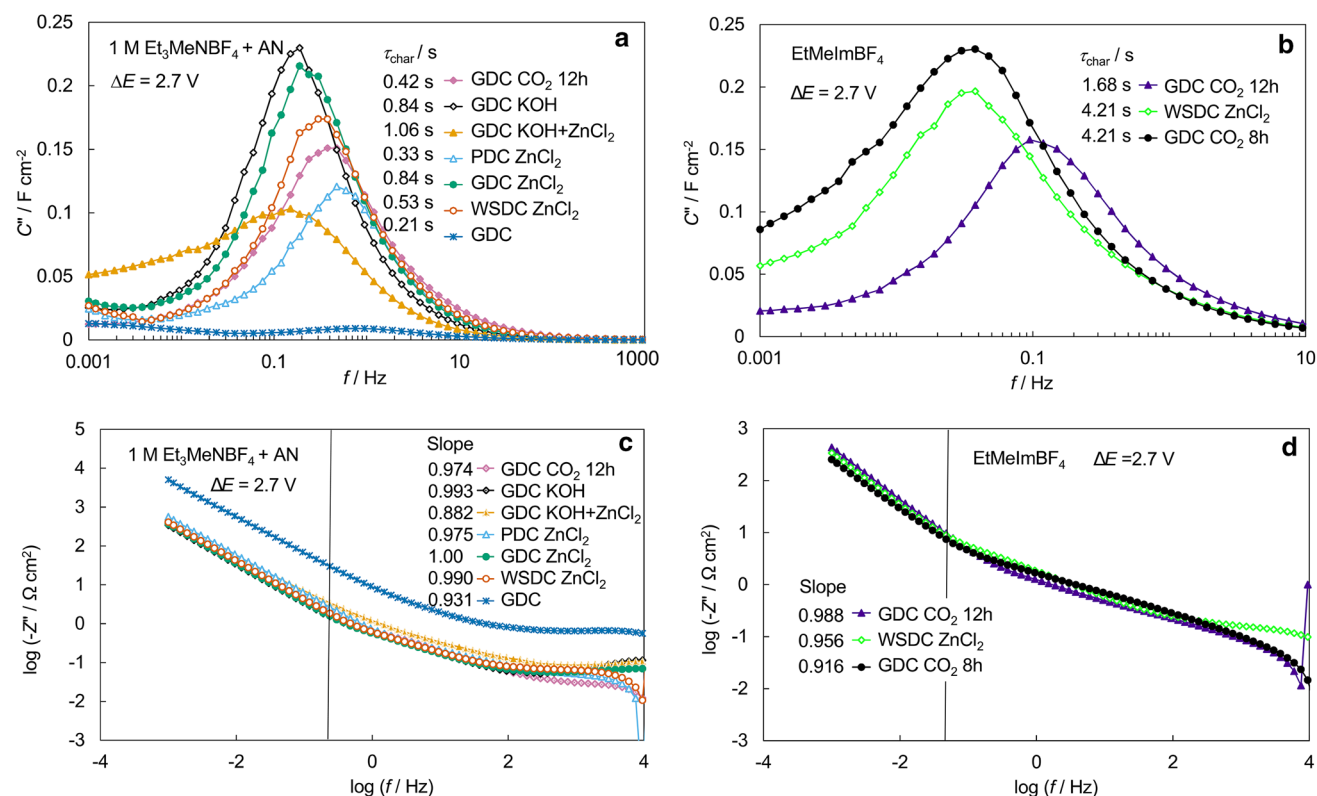

Fig. 8 Imaginary part of capacitance versus ac frequency plots for the EDLCs based on the different carbon materials (noted in the figure) in Et$_3$MeNBF$_4$ in AN (**a**) and EtMeImBF$_4$ ionic liquid (**b**), logarithmical negative values of imaginary part of impedance versus loga-rithmical ac frequency plots for the EDLCs based on the different carbon materials (noted in the figure) in Et$_3$MeNBF$_4$ in AN (**c**) and EtMeImBF$_4$ ionic liquid (**d**)
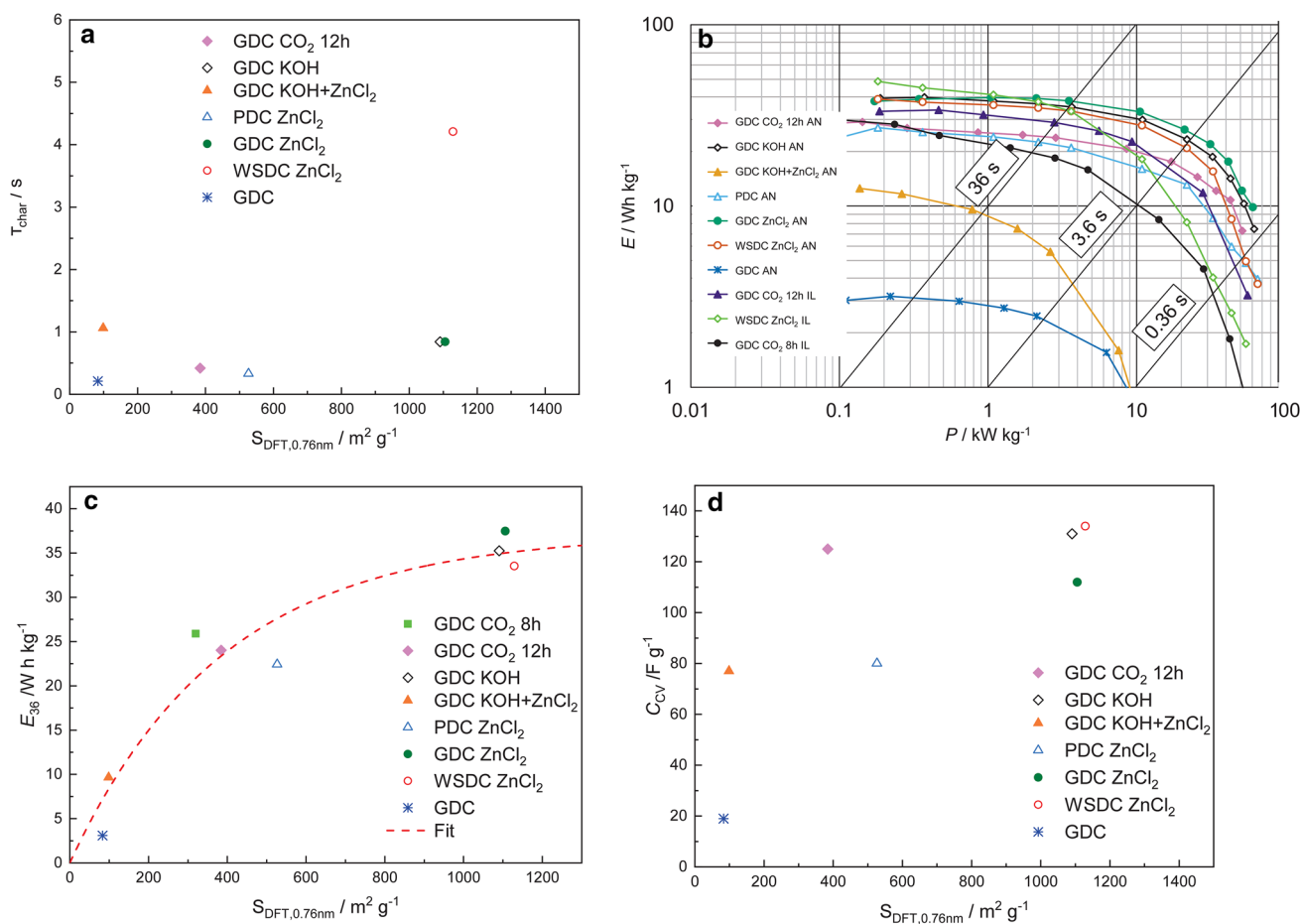
Fig. 9 Characteristic time constant (Table 3) versus specific surface area plot calculated for materials with pores widths larger than 0.76 nm, which was calculated by fitting 2D-NLDFT-HS model to the N_2 adsorption data and subtracting pores smaller than 0.76 nm (**a**); specific energy versus specific power plots for the EDLCs based on the different carbon material (**b**) with 1 M Et_3MeNBF_4 in AN and EtMeImBF$_4$ ionic liquid electrolytes (noted in figure), specific power and specific energy values were obtained from constant power discharge tests within the cell potential range from 3.0 to 1.5 V; energy density discharging time of 36 s (E_{36}) versus $S_{DFT,0.76nm}$ plots (**c**); integrated capacitance (Table 3) versus specific surface area (from pores with widths larger than 0.76 nm) plot (**d**)

have the shortest charging/discharging times, because there is no larger micropores/mesopores in needful quantities for quick mass-transfer of ions in porous structured the very energy-dense carbon materials EDLC. Based on the analysis conducted, the τ_{char} values characterize the mass-transfer processes (rate) in mesopores/larger micropores and only at very low ac frequencies, the finite-length adsorption processes control the EDLC behaviour (Fig. 7).

The $\log|-Z''|$ versus $\log(f)$ dependences have been constructed (absolute values of slopes are given in Fig. 8c, d), and there are very long linear areas with slope values more negative than -0.98 were established at low ac frequency region. Nearly ideal capacitive behaviour (slope $= -1.0$ is the characteristic of the ideally polarizable electrode) has been observed up to 2.7 V cell potentials [8, 61]. At higher cell potentials, somewhat less negative slope values for $\log|-Z''|$ versus $\log(f)$ have been obtained indicating

the increasing rate of faradic processes at $\Delta E > 3.2$ V. The shape of $\log|-Z''|$ versus $\log(f)$ plots depends noticeably on the electrolyte used and for EtMeImBF$_4$, less negative slope values (-0.96) at $f = 1$ mHz have been calculated indicating that very weak deviation from the adsorption step limited mechanism towards mixed kinetics (adsorption and mass-transfer limited steps) is possible.

3.7 Ragone plots

Ragone plots for EDLC have been measured using the constant power discharge method. Data in Fig. 9b show that the highest energy densities (at fixed power densities) have been measured for WSDC $ZnCl_2$ in EtMeImBF$_4$, having highest C_s values (S_{BET} at high mesopore/micropore). Only very slightly lower energy densities have been measured for GDC CO_2 12 h, WSDC $ZnCl_2$ and GDC KOH or GDC $ZnCl_2$.

For mainly microporous GDC CO_2 8 h or GDC, lower energy densities have been measured. It is very well visible that in the high power density region, the GDC CO_2 12 h, GDC KOH or GDC $ZnCl_2$ surpasses the WSDC $ZnCl_2$ carbon-based ionic liquid cell energy and power densities.

Thus, for high power density, EDLC materials with an optimal ratio of micropores and mesopores in the carbon powder are necessary. Therefore, hierarchically micro–mesoporous systems should be used, where quick mass-transfer is possible in the porous electrode matrix. There is no big difference in energy densities for 1 M Et_3MeNBF_4 in AN, and $EtMeImBF_4$-based EDLCs at longer discharge times (lower $P \leq 10$ kW kg^{-1}). At shorter discharge times ($P \geq 10$ kW kg^{-1}), noticeably lower power densities have been measured for $EtMeImBF_4$-based EDLC explained by higher mass-transfer resistance values for viscous $EtMeImBF_4$. Energy densities at a discharging time of 36 s (E_{36}) versus the available specific surface area, $S_{DFT,0.76nm}$, for the systems investigated are presented in Fig. 9c. The available surface area was calculated by subtracting the specific surface area from pores smaller than 0.76 nm from the S_{DFT} value calculated by fitting the N_2 adsorption isotherm with the 2D-NLDFT-HS model using SAIEUS software [8, 66, 79]. The lower accessible pore size of 0.76 nm has been based on the modelled ion sizes of the $(C_2H_5)_3CH_3N^+$ and BF_4^- ions [80] and on the analysis of surface characteristics influence on the energy storage capability of multiple systems conducted in Ref. [8]. Discharging time of 36 s corresponds to nearly maximal reachable energy density, visible from Ragone plots (Fig. 9b), except in the case of GDC KOH + $ZnCl_2$-based and $EtMeImBF_4$-based EDLC. The dependence of the E_{36} values on the $S_{DFT,0.76nm}$ is asymptotical, i.e. with the increase of available specific surface area the E_{36} scales up towards a limiting value. This dependence has been fitted with a Box-Lucas type equation: $E_{36} = a\left(1 - e^{\left(-b*S_{DFT,0.76nm}\right)}\right)$ (Fig. 9c, dashed line). The fit results are $a = 37.2 \pm 3.4$ W h kg^{-1}, which characterizes the maximal achievable E_{36} with increased $S_{DFT,0.76nm}$, and $b = 0.00258 \pm 0.00064$ g m^{-2}.

The integral capacitance values established from CV data by calculating the total discharged charge according to Eq. (7), C_{CV}, which was measured from cell potential 0 V up to 3.0 V at $v = 1$ mV s^{-1} versus the accessible specific surface area, $S_{DFT,0.76nm}$, are presented in Fig. 9d. Overall the dependence of C_{CV} on the $S_{DFT,0.76nm}$ is similar to the dependence of the E_{36} on the $S_{DFT,0.76nm}$, with the exception of GDC KOH + $ZnCl_2$-based EDLC. The large difference in the values of E_{36} and C_{CV} for GDC KOH and GDC $ZnCl_2$-based EDLCs is caused by the limited available energy density achievable from constant power discharge performed at 36 s, E_{36}. This effect is also visible from the Ragone plots (Fig. 9b), where the total energy density of GDC increases remarkably, from 9.6 W h kg^{-1} at 33 s to 12.5 W h kg^{-1} at 250 s, with longer discharging times at lower power densities. This is caused by the mostly ultramicro-porous structure of GDC KOH + $ZnCl_2$ (Fig. 3c), which limits the diffusion, i.e. mass-transfer rate of ions in this EDLC.

4 Conclusions

Activated carbon materials were synthesized from an organic carbon-containing material. The aqueous solutions of D-glucose and granulated white sugar were hydrothermally carbonized. The resulting materials and Estonian highly decomposed peat were thereafter activated with KOH, CO_2 or $ZnCl_2$ (in various mass ratios or time) to enhance the micro- and mesoporosity.

Based on the XRD and Raman spectroscopy data, the synthesized carbon materials are mainly amorphous. N_2 sorption measurements results show that the activated carbon materials are mainly microporous. However, KOH and $ZnCl_2$ activation steps yield carbons that contain also reasonable amount of smaller mesopores, where the Brunauer–Emmett–Teller (BET)-specific surface area were up to $S_{BET} = 2150$ m^2 g^{-1}, micropore pore volume values up to $V_{micro} = 1.01$ cm^3 g^{-1} and total pore volume values up to $V_{tot} = 1.05$ cm^3 g^{-1}.

The electrochemical characteristics of the EDLCs consisting of the differently activated carbon materials-based electrodes in 1 M triethylmethylammonium tetrafluoroborate (Et_3MeNBF_4) solution in acetonitrile (AN) and in 1-ethyl-3-methylimidazolium tetrafluoroborate ionic liquid ($EtMeImBF_4$) were tested applying the electrochemical impedance spectroscopy, cyclic voltammetry, constant current charge/discharge and the constant power discharge methods.

The electrochemical measurement results show that the values of specific capacitance are significantly different for the best cells with high capacitance for $EtMeImBF_4$ (144 F g^{-1}) electrolyte compared to the 1 M Et_3MeNBF_4 in AN (134 F g^{-1}). Very low capacitance values (20 F g^{-1}) have been measured for non-activated GDC and PDC.

The specific energy versus specific power dependence data strongly depend on the carbon materials used. At low constant power value (10 W h kg^{-1}), the stored energy is higher for EDLC based on $EtMeImBF_4$ ionic liquid (48 W h kg^{-1}) compared with EDLC based on Et_3MeNBF_4 solution in AN (39 W h kg^{-1}). However, the best capacitance retention and shortest relaxation time constants $\tau_{char} \sim 0.42$ s and 0.53 s were established for EDLCs with 1 M Et_3MeNBF_4 solution in AN due to the lower viscosity and higher electrical conductivity compared to the ionic

liquid-based electrolytes. Thus, the EDLC based on 1 M Et_3MeNBF_4 solution in AN electrolyte and using for completing the EDLC deliver substantially higher energy at higher constant power values ($P \geq 10$ kW kg^{-1}).

The carbon materials synthesized using cheap and abundant granulated white sugar and Estonian highly decomposed peat show good electrochemical performance in 1 M Et_3MeNBF_4 in AN, as well as in $EtMeImBF_4$ ionic liquid and are promising carbon materials for completing the high energy and power density supercapacitors. It is important to mention that the synthesis of carbon nanospheres is simpler and environmentally friendlier than the preparation of molybdenum carbide or titanium carbide-derived carbon powders. However, the optimization of peat- and white sugar-derived carbon materials needs future detailed complex studies.

Compliance with Ethical Standards

Conflict of interest The authors declare that they have no conflict of interest.

References

1. Conway BE (1999) Electrochemical supercapacitors: scientific fundamentals and technological applications. Springer, New York
2. Kötz R, Carlen M (2000) Principles and applications of electrochemical capacitors. Electrochim Acta 45:2483–2498
3. Burke A, Miller M (2011) The power capability of ultracapacitors and lithium batteries for electric and hybrid vehicle applications. J Power Sources 196:514–522
4. Frackowiak E, Beguin F (2001) Carbon materials for the electrochemical storage of energy in capacitors. Carbon 39:937–950
5. Scrosati B, Hassoun J, Sun Y-K (2011) Lithium-ion batteries. A look into the future. Energy Environ Sci 4:3287–3295
6. Gogotsi Y, Nikitin A, Ye H et al (2003) Nanoporous carbide-derived carbon with tunable pore size. Nat Mater 2:591–594
7. Zuo W, Li R, Zhou C et al (2017) Battery-supercapacitor hybrid devices: recent progress and future prospects. Adv Sci 4:1600359
8. Härmas R, Palm R, Härmas M et al (2018) Influence of porosity parameters and electrolyte chemical composition on the power densities of non-aqueous and ionic liquid based supercapacitors. Electrochim Acta 283:931–948
9. Laheäär A, Przygocki P, Abbas Q, Béguin F (2015) Appropriate methods for evaluating the efficiency and capacitive behavior of different types of supercapacitors. Electrochem Commun 60:21–25
10. Pohl M, Tallo I, Jänes A et al (2018) Increasing the stability of very high potential electrical double layer capacitors by operando passivation. J Power Sources 402:53–61
11. Goodenough JB (2015) Energy storage materials: a perspective. Energy Storage Mater 1:158–161
12. Singhal SC (2014) Solid oxide fuel cells for power generation. Wiley Interdiscip Rev Energy Environ 3:179–194
13. Tallo I, Thomberg T, Kurig H et al (2013) Supercapacitors based on carbide-derived carbons synthesised using HCl and Cl$_2$ as reactants. J Solid State Electrochem 17:19–28
14. Tee E, Tallo I, Kurig H et al (2015) Huge enhancement of energy storage capacity and power density of supercapacitors based on the carbon dioxide activated microporous SiC-CDC. Electrochim Acta 161:364–370
15. Tee E, Tallo I, Thomberg T et al (2016) Supercapacitors based on activated silicon carbide-derived carbon materials and ionic liquid. J Electrochem Soc 163:A1317–A1325
16. Laheäär A, Jänes A, Lust E (2011) Electrochemical properties of carbide-derived carbon electrodes in non-aqueous electrolytes based on different Li-salts. Electrochim Acta 56:9048–9055
17. Tallo I, Thomberg T, Kontturi K et al (2011) Nanostructured carbide-derived carbon synthesized by chlorination of tungsten carbide. Carbon 49:4427–4433
18. Taberna PL, Simon P, Fauvarque JF (2003) Electrochemical characterics and impedance spectroscopy studies of carbon-carbon supercapacitors. J Electrochem Soc 150:A292–A300
19. Jänes A, Permann L, Arulepp M, Lust E (2004) Electrochemical characteristics of nanoporous carbide-derived carbon materials in non-aqueous electrolyte solutions. Electrochem Commun 6:313–318
20. Thomberg T, Jänes A, Lust E (2009) Energy and power performance of vanadium carbide derived carbon electrode materials for supercapacitors. J Electroanal Chem 630:55–62
21. Kockrick E, Schrage C, Borchardt L et al (2010) Ordered mesoporous carbide derived carbons for high pressure gas storage. Carbon 48:1707–1717
22. Sepp S, Härk E, Valk P et al (2014) Impact of the Pt catalyst on the oxygen electroreduction reaction kinetics on various carbon supports. J Solid State Electrochem 18:1223–1229
23. Lust E, Vaarmets K, Nerut J et al (2014) Influence of specific surface area and microporosity-mesoporosity of pristine and Pt-nanoclusters modified carbide derived carbon electrodes on the oxygen electroreduction. Electrochim Acta 140:294–303
24. Lust E, Tamm K, Nurk G et al (2015) Development of medium-temperature solid oxide fuel cells and CO$_2$ and H$_2$O co-electrolysis cells in Estonia. ECS Trans 68:3407–3415
25. Varin R, Czujko T, Wronski Z, Zaranski Z (2009) Nanomaterials for hydrogen storage produced by ball milling. Can Metall Q 48:11–25
26. Palm R, Kurig H, Aruväli J, Lust E (2018) NaAlH$_4$/microporous carbon composite materials for reversible hydrogen storage. Microporous Mesoporous Mater 264:8–12
27. Tõnurist K, Thomberg T, Jänes A, Lust E (2013) Specific performance of supercapacitors at lower temperatures based on different separator materials. J Electrochem Soc 160:A449–A457
28. Tõnurist K, Thomberg T, Jänes A et al (2012) Specific performance of electrical double layer capacitors based on different separator materials in room temperature ionic liquid. Electrochem Commun 22:77–80
29. Irvine JTS, Neagu D, Verbraeken MC et al (2016) Evolution of the electrochemical interface in high-temperature fuel cells and electrolysers. Nat Energy 1:15014
30. Thomberg T, Tooming T, Romann T et al (2013) High power density supercapacitors based on the carbon dioxide activated ᴅ-glucose derived carbon electrodes and acetonitrile electrolyte. J Electrochem Soc 160:A1834–A1841
31. Härmas M, Thomberg T, Romann T et al (2017) Carbon for energy storage derived from granulated white sugar by hydrothermal carbonization and subsequent zinc chloride activation. J Electrochem Soc 164:A1866–A1872

32. Tooming T, Thomberg T, Siinor L et al (2014) A type high capacitance supercapacitor based on mixed room temperature ionic liquids containing specifically adsorbed iodide anions. J Electrochem Soc 161:A222–A227

33. Eskusson J, Jänes A, Kikas A et al (2011) Physical and electrochemical characteristics of supercapacitors based on carbide derived carbon electrodes in aqueous electrolytes. J Power Sources 196:4109–4116

34. Jänes A, Eskusson J, Mattisen L, Lust E (2014) Electrochemical behaviour of hybrid devices based on Na_2SO_4 and Rb_2SO_4 neutral aqueous electrolytes and carbon electrodes within wide cell potential region. J Solid State Electrochem 19:769–783

35. Eskusson J, Rauwel P, Nerut J, Jänes A (2016) A hybrid capacitor based on Fe_3O_4-graphene nanocomposite/few-layer graphene in different aqueous electrolytes. J Electrochem Soc 163:A2768–A2775

36. Laheäär A, Jänes A, Lust E (2012) $NaClO_4$ and $NaPF_6$ as potential non-aqueous electrolyte salts for electrical double layer capacitor application. Electrochim Acta 82:309–313

37. Sigalov S, Levi MD, Salitra G et al (2012) Selective adsorption of multivalent ions into TiC-derived nanoporous carbon. Carbon 50:3957–3960

38. Laheäär A, Jänes A, Lust E (2014) Cesium carborane as an unconventional non-aqueous electrolyte salt for electrochemical capacitors. Electrochim Acta 125:482–487

39. Laheäär A, Peikolainen A-L, Koel M et al (2012) Comparison of carbon aerogel and carbide-derived carbon as electrode materials for non-aqueous supercapacitors with high performance. J Solid State Electrochem 16:2717–2722

40. Kurig H, Jänes A, Lust E (2010) Electrochemical characteristics of carbide-derived carbon|1-ethyl-3-methylimidazolium tetrafluoroborate supercapacitor cells. J Electrochem Soc 157:A272–A279

41. Pohl M, Kurig H, Tallo I et al (2017) Novel sol-gel synthesis route of carbide-derived carbon composites for very high power density supercapacitors. Chem Eng J 320:576–587

42. Härmas M, Thomberg T, Kurig H et al (2016) Microporous–mesoporous carbons for energy storage synthesized by activation of carbonaceous material by zinc chloride, potassium hydroxide or mixture of them. J Power Sources 326:624–634

43. Kurig H, Vestli M, Tõnurist K et al (2012) Influence of room temperature ionic liquid anion chemical composition and electrical charge delocalization on the supercapacitor properties. J Electrochem Soc 159:A944–A951

44. Daikhin LI, Kornyshev AA, Urbakh M (1996) Double-layer capacitance on a rough metal surface. Phys Rev E 53:6192–6199

45. Daikhin LI, Kornyshev AA, Urbakh M (1998) Nonlinear Poisson-Boltzmann theory of a double layer at a rough metal/electrolyte interface: a new look at the capacitance data on solid electrodes. J Chem Phys 108:1715–1723

46. Daikhin LI, Kornyshev AA, Urbakh M (1997) Double layer capacitance on a rough metal surface: surface roughness measured by "Debye ruler". Electrochim Acta 42:2853–2860

47. Lust E, Jänes A, Sammelselg V, Miidla P (2000) Influence of charge density and electrolyte concentration on the electrical double layer characteristics at rough cadmium electrodes. Electrochim Acta 46:185–191

48. Kornyshev AA (2007) Double-layer in ionic liquids: paradigm change? J Phys Chem B 111:5545–5557

49. Ivaništšev V, O'Connor S, Fedorov MV (2014) Poly(a)morphic portrait of the electrical double layer in ionic liquids. Electrochem Commun 48:61–64

50. Kornyshev AA, Luque NB, Schmickler W (2014) Differential capacitance of ionic liquid interface with graphite: the story of two double layers. J Solid State Electrochem 18:1345–1349

51. Pallarés J, González-Cencerrado A, Arauzo I (2018) Production and characterization of activated carbon from barley straw by physical activation with carbon dioxide and steam. Biomass Bioenergy 115:64–73

52. Kormann M, Popovska N (2010) Processing of carbide-derived carbons with enhanced porosity by activation with carbon dioxide. Microporous Mesoporous Mater 130:167–173

53. Li Z-Y, Akhtar MS, Kwak D-H, Yang O-B (2017) Improvement in the surface properties of activated carbon via steam pretreatment for high performance supercapacitors. Appl Surf Sci 404:88–93

54. Zhao Q, Wang X, Liu J et al (2015) Surface modification and performance enhancement of carbon derived from chromium carbide for supercapacitor applications. J Electrochem Soc 162:A845–A851

55. Lobato B, Suárez L, Guardia L, Centeno TA (2017) Capacitance and surface of carbons in supercapacitors. Carbon 122:434–445

56. Zhang Y-J, Xing Z-J, Duan Z-K et al (2014) Effects of steam activation on the pore structure and surface chemistry of activated carbon derived from bamboo waste. Appl Surf Sci 315:279–286

57. Presser V, Heon M, Gogotsi Y (2011) Carbide-derived carbons—from porous networks to nanotubes and graphene. Adv Funct Mater 21:810–833

58. Román S, González JF, González-García CM, Zamora F (2008) Control of pore development during CO_2 and steam activation of olive stones. Fuel Process Technol 89:715–720

59. Osswald S, Portet C, Gogotsi Y et al (2009) Porosity control in nanoporous carbide-derived carbon by oxidation in air and carbon dioxide. J Solid State Chem Fr 182:1733–1741

60. Eikerling M, Kornyshev AA, Lust E (2005) Optimized structure of nanoporous carbon-based double-layer capacitors. J Electrochem Soc 152:E24–E33

61. Tooming T, Thomberg T, Kurig H et al (2015) High power density supercapacitors based on the carbon dioxide activated D-glucose derived carbon electrodes and 1-ethyl-3-methylimidazolium tetrafluoroborate ionic liquid. J Power Sources 280:667–677

62. Bisquert J (2000) Infuence of the boundaries in the impedance of porous film electrodes. Phys Chem Chem Phys 2:4185–4192

63. Titirici M-M (2013) Sustainable carbon materials from hydrothermal processes. Wiley, Chichester

64. Brunauer S, Emmett PH, Teller E (1938) Adsorption of gases in multimolecular layers. J Am Chem Soc 60:309–319

65. Jagiello J, Ania C, Parra JB, Cook C (2015) Dual gas analysis of microporous carbons using 2D-NLDFT heterogeneous surface model and combined adsorption data of N_2 and CO_2. Carbon 91:330–337

66. Jagiello J, Olivier JP (2013) 2D-NLDFT adsorption models for carbon slit-shaped pores with surface energetical heterogeneity and geometrical corrugation. Carbon 55:70–80

67. Sevilla M, Fuertes AB (2011) Sustainable porous carbons with a superior performance for CO_2 capture. Energy Environ Sci 4:1765–1771

68. Tuinstra F, Koenig JL (1970) Raman spectrum of graphite. J Chem Phys 53:1126–1130

69. Ferrari AC (2007) Raman spectroscopy of graphene and graphite: disorder, electron–phonon coupling, doping and nonadiabatic effects. Solid State Commun 143:47–57

70. Dresselhaus MS, Dresselhaus G, Hofmann M (2007) The big picture of Raman scattering in carbon nanotubes. Vib Spectrosc 45:71–81

71. Kurig H, Russina M, Tallo I et al (2016) The suitability of infinite slit-shaped pore model to describe the pores in highly porous carbon materials. Carbon 100:617–624

72. Pimenta MA, Dresselhaus G, Dresselhaus MS et al (2007) Studying disorder in graphite-based systems by Raman spectroscopy. Phys Chem Chem Phys 9:1276–1290

73. Ferrari AC, Meyer JC, Scardaci V et al (2006) Raman spectrum of graphene and graphene layers. Phys Rev Lett 97:187401
74. Thomberg T, Kurig H, Jänes A, Lust E (2011) Mesoporous carbide-derived carbons prepared from different chromium carbides. Microporous Mesoporous Mater 141:88–93
75. Li Q-Y, Wang H-Q, Dai Q-F et al (2008) Novel activated carbons as electrode materials for electrochemical capacitors from a series of starch. Solid State Ion 179:269–273
76. Chmiola J, Yushin G, Dash R, Gogotsi Y (2006) Effect of pore size and surface area of carbide derived carbons on specific capacitance. J Power Sources 158:765–772
77. Salitra G, Soffer A, Eliad L et al (2000) Carbon electrodes for double-layer capacitors I. Relations between ion and pore dimensions. J Electrochem Soc 147:2486–2493
78. Wei L, Sevilla M, Fuertes AB et al (2011) Hydrothermal carbonization of abundant renewable natural organic chemicals for high-performance supercapacitor electrodes. Adv Energy Mater 1:356–361
79. Jagiello J (1994) Stable numerical solution of the adsorption integral equation using splines. Langmuir 10:2778–2785
80. Jänes A, Kurig H, Romann T, Lust E (2010) Novel doubly charged cation based electrolytes for non-aqueous supercapacitors. Electrochem Commun 12:535–539

Affiliations

M. Härmas[1] · R. Palm[1] · T. Thomberg[1] · R. Härmas[1] · M. Koppel[1] · M. Paalo[1] · I. Tallo[1] · T. Romann[1] · A. Jänes[1] · E. Lust[1]

M. Härmas
meelis.harmas@ut.ee

R. Palm
rasmus.palm@ut.ee

R. Härmas
riinu.harmas@ut.ee

M. Koppel
miriam.koppel@ut.ee

M. Paalo
maarja.paalo@ut.ee

I. Tallo
indrek.tallo@ut.ee

T. Romann
tavo.romann@ut.ee

A. Jänes
alar.janes@ut.ee

E. Lust
enn.lust@ut.ee

[1]   Institute of Chemistry, University of Tartu, 50411 Tartu, Estonia